JGR Space Physics

RESEARCH ARTICLE
10.1029/2020JA028215

Special Section:
Geospace Multi-Point Observations in Van Allen Probes and Arase Era

Dynamic Properties of Particle Injections Inside Geosynchronous Orbit: A Multisatellite Case Study

T. Motoba[1], S. Ohtani[1], S. G. Claudepierre[2,3], G. D. Reeves[4], A. Y. Ukhorskiy[1], and L. J. Lanzerotti[5]

[1]The Johns Hopkins University Applied Physics Laboratory, Laurel, MD, USA, [2]Space Sciences Department, Aerospace Corporation, Los Angeles, CA, USA, [3]Department of Atmospheric and Oceanic Sciences, University of California, Los Angeles, CA, USA, [4]Los Alamos National Laboratory, Los Alamos, NM, USA, [5]Center for Solar-Terrestrial Research, New Jersey Institute of Technology, Newark, NJ, USA

Key Points:
- Four spacecraft observations at and inside GEO reveal the dynamical nature of particle injections and their related local field changes
- The dispersionless injections inside GEO are highly localized in azimuth and accompanied by a sharp dipolarization front (DF)
- The DF-related fields have a much greater impact on electron and light ion injections, but little affect heavy ion injections

Correspondence to:
T. Motoba,
tetsuo.motoba@gmail.com

Citation:
Motoba, T., Ohtani, S., Claudepierre, S. G., Reeves, G. D., Ukhorskiy, A. Y., & Lanzerotti, L. J. (2020). Dynamic properties of particle injections inside geosynchronous orbit: A multisatellite case study. *Journal of Geophysical Research: Space Physics*, *125*, e2020JA028215. https://doi.org/10.1029/2020JA028215

Received 13 MAY 2020
Accepted 29 AUG 2020
Accepted article online 3 SEP 2020

Abstract Four closely located satellites at and inside geosynchronous orbit (GEO) provided a great opportunity to study the dynamical evolution and spatial scale of premidnight energetic particle injections inside GEO during a moderate substorm on 23 December 2016. Just following the substorm onset, the four spacecraft, a LANL satellite at GEO, the two Van Allen Probes (also called "RBSP") at ~5.8 R_E, and a THEMIS satellite at ~5.3 R_E, observed substorm-related particle injections and local dipolarizations near the central meridian (~22 MLT) of a wedge-like current system. The large-scale evolution of the electron and ion (H, He, and O) injections was almost identical at the two RBSP spacecraft with ~0.5 R_E apart. However, the initial short-timescale particle injections exhibited a striking difference between RBSP-A and -B: RBSP-B observed an energy dispersionless injection which occurred concurrently with a transient, strong dipolarization front (DF) with a peak-to-peak amplitude of ~25 nT over ~25 s; RBSP-A measured a dispersed/weaker injection with no corresponding DF. The spatiotemporally localized DF was accompanied by an impulsive, westward electric field (~20 mV m^{-1}). The fast, impulsive $\mathbf{E} \times \mathbf{B}$ drift caused the radial transport of the electron and ion injection regions from GEO to ~5.8 R_E. The penetrating DF fields significantly altered the rapid energy- and pitch angle-dependent flux changes of the electrons and the H and He ions inside GEO. Such flux distributions could reflect the transient DF-related particle acceleration and/or transport processes occurring inside GEO. In contrast, O ions were little affected by the DF fields.

1. Introduction

Particle injections, characterized as sudden enhancements of energetic particle fluxes in the near-Earth tail and inner magnetosphere, are one of the most important and well-known manifestations of the expansion onset of magnetospheric substorms. The enhanced energetic particle fluxes can either be formed due to a local acceleration, or can be accelerated in a more tailward region and then become further accelerated during their inward transport. Magnetic field dipolarizations around substorm onset are a powerful source of particle acceleration, responsible for transporting energetic particles into the inner magnetosphere. The extensive studies of injections and dipolarizations have been done using the geosynchronous spacecraft located at 6.6 R_E (e.g., Birn et al., 1997a, 1997b, 1998; Kokubun & McPherron, 1981; Nagai, 1982; Reeves et al., 1990, 1991). On the other hand, a launch of the CRRES (Combined Release and Radiation Effects Satellite) mission in 1990 provided a new opportunity to study injections and dipolarizations inside geosynchronous orbit (GEO), although the mission lifetime was only ~15 months (Fu et al., 2002; Maynard et al., 1996; Sergeev et al., 1998). Further studies of injections and dipolarizations inside GEO have been followed by observations from the twin satellite Van Allen Probes mission (formerly named the Radiation Belt Storm Probes: RBSP) launched in 2012 (e.g., Dai et al., 2015; Gkioulidou et al., 2015; Malaspina et al., 2015; Turner et al., 2015). Recent statistical results from the RBSP mission showed the responses of energetic particles to local dipolarizations inside GEO by performing a superposed epoch analysis (Liu et al., 2016; Motoba et al., 2018, 2020; Nosé et al., 2016). Whereas these statistical results yielded the average picture of the energy-, species-, and charge-state-dependent behaviors of particle injections associated with local dipolarizations, they did not capture the dynamic evolution of injections and dipolarizations and their spatial extent.

Dipolarizations inside GEO are observed in two different ways: (1) sustained (large-scale) dipolarizations with a lifetime of 30 min or longer (Ohtani et al., 2018), and (2) transient (pulse-like) dipolarizations with

a lifetime of the order of minutes (the so-called dipolarization fronts, DFs) (Liu et al., 2016). Sustained dipolarizations are usually observed at GEO or even closer to Earth, and considered to be a manifestation of large-scale substorm current wedge formation. DFs, on the other hand, are usually observed in the magnetotail plasma sheet beyond GEO, carry field-aligned currents (FACs) that form a current "wedgelet," and occur concurrently with transient, spatially localized high-speed plasma flows (called bursty bulk flows [BBF], or flow bursts) which play a major role in the magnetotail mass, energy, and magnetic flux transport. DFs in the magnetotail are accompanied not only by a transiently enhanced electric field, but also by dispersionless particle injections (e.g., Gabrielse et al., 2012, 2014). A recent numerical simulation by Merkin et al. (2019) has demonstrated that a direct impact by a deeply penetrating DF results in a sharp geosynchronous dipolarization, while geosynchronous dipolarization longitudinally away from the DF meridian becomes much more gradual. A similar conclusion has been drawn by Gkioulidou et al. (2015) when examining premidnight dipolarizations measured by RBSP.

However, observations by two radially separated spacecraft have indicated that only a small portion of flow bursts (or DFs) in the magnetotail have a clear linkage with near-Earth and geosynchronous dipolarizations (Dubyagin et al., 2011; Ohtani et al., 2006; Takada et al., 2006). The observational fact has spurred an ongoing debate, which is whether sustained dipolarizations are an accumulation of DFs which penetrate deeper than the flow-breaking region. For instance, Liu et al. (2015) hypothesized that a large-scale substorm current wedge is the combined effect of many wedgelets associated with mesoscale DFs, based on the statistical distribution of wedgelets in the dawn and dusk sectors of the magnetotail. Ohtani and Gjerloev (2020), however, found that throughout the nightside, the magnitude of midlatitude positive bays changes in correlation with the SML index, SuperMAG equivalent to AL, and therefore, they concluded that as a first approximation the substorm current system is a globally coherent system rather than an ensemble of wedgelets. In terms of the amount of magnetic flux transport, on the other hand, Lui (2015) doubted that penetrating DFs play a significant role in the formation of near-Earth dipolarization, because the accumulated flux transport within the DFs is insufficient in supplementing magnetic flux increase in the sustained dipolarization in the near-Earth region. However, this appears to contradict the recent numerical prediction by Merkin et al. (2019), who showed that a global, sustained substorm dipolarization in the inner magnetosphere (within 8 R_E) is a result of an accumulation of many azimuthally localized DFs.

The particle acceleration and transport processes for injections are a subject of ongoing research. By investigating the dynamics of single-particle trajectories in simulations of the substorm expansion phase with focus on ions, Delcourt (2002) demonstrated that the nonadiabatic ion behavior in the magnetotail can lead to dramatic local acceleration, mainly in the perpendicular direction. Particularly, since heavy ions with larger Larmor radii are unmagnetized more easily, they are considered to get much more energized by local electric field accompanying dipolarization (or DF) in the plasma sheet. Birn et al. (1997a, 1998), by tracing test particle orbits in the dynamic fields of a three-dimensional MHD simulation of dipolarization in the magnetotail, found that most energized particles experience betatron acceleration as the particles are transported into a stronger magnetic field region by a dipolarization-related dawn-dusk electric field. On the other hand, in situ pitch angle observations have shown that DF-induced energetic particle flux enhancement in the magnetotail is caused by betatron acceleration, Fermi acceleration, or a combination of them, depending on whether the spacecraft location is close to or far from the equatorial plane (Runov et al., 2013), and on whether the particle enhancement occurs inside the growing or decaying flux pileup region (Fu et al., 2011).

Because of significant differences between the ambient magnetic field and the DF properties in the magnetotail and the inner magnetosphere, however, the physical mechanisms of particle acceleration at DF in the inner magnetosphere may be different from those in the magnetotail. Recent high-resolution MHD/particle simulations have demonstrated that some mesoscale flow bursts (or DFs) can penetrate inside GEO and that they drive particle injections responsible for the buildup of ring current ions and radiation belt electrons (Sorathia et al., 2018; Ukhorskiy et al., 2017, 2018). The simulations have also introduced a new energization process for which the stable magnetic trapping of energetic particles at each of the DFs can potentially accelerate the particle population in the inner magnetosphere, even in the absence of large electric fields. However, it remains to be understood observationally about the dynamical behavior of energetic particles in deeply penetrating DFs, particularly the energy-, species-, and pitch angle-dependent properties.

In this study we investigate the dynamic evolution of energetic particle injections inside GEO during a substorm event on 23 December 2016, by combining fields and energetic particles data from multipoint spacecraft being located closely at and inside GEO near the onset meridian and ground-based magnetometer data from various stations. In the initial stage of the injections that occurred concurrently with local dipolarizations, the electron and ion dispersionless injections accompanying a sharp, transient DF were observed only by one of the two RBSP spacecraft which traveled near apogee with a small azimuthal separation of ~0.5 R_E, corresponding to ~20 min in magnetic local time (MLT). By comparing and differentiating the simultaneous observations at the two RBSP spacecraft, we seek to examine the impact of the highly localized DF on energetic particles inside GEO.

The remainder of the paper is organized as follows. Section 2 describes the instrumentation and data. Section 3 presents the observations. Section 4 presents discussion, and section 5 gives conclusions of this study.

2. Instrumentation and Data

In this study we primarily used data from NASA's Van Allen Probes (RBSP) mission, consisting of two identically instrumented spacecraft with apogee of 5.8 R_E, perigee of ~600 km, and an orbital period of 9 hr (Mauk et al., 2013). The data are taken from the four different instruments: Electric and Magnetic Field Instrument Suite and Integrated Science (EMFISIS) instrument (Kletzing et al., 2013); Electric Fields and Waves (EFW) instrument (Wygant et al., 2013); Radiation Belt Storm Probes Ion Composition Experiment (RBSPICE, Mitchell et al., 2013); and Magnetic Electron Ion Spectrometer (MagEIS, Blake et al., 2013) that is part of the Energetic Particle, Composition, and Thermal Plasma Suite (ECT, Spence et al., 2013). We use the 1-s averaged data of magnetic field vectors measured by EMFISIS. The magnetic field data are converted into the *VDH* coordinate system, in which *H* (northward) is antiparallel to the geomagnetic dipole axis, *D* (positive eastward) is perpendicular to the local dipole meridian, and *V* (radially outward) is the radial component and parallel to the magnetic equator. The *VDH* coordinate system is widely used for identifying the transition of the magnetic field configuration from tail-like to dipole-like (or vice versa) in the inner magnetosphere, where the terrestrial dipole field is dominant. EFW consists of two orthogonal centripetally deployed booms in the spin plane with tip-to-tip separations of 100 m to measure electric field vectors in the spin plane at a cadence of 32 samples per second. The electric field data are represented in the Modified Geocentric Solar Ecliptic (MGSE) coordinate system, which is a near GSE coordinate system. In this study the *y* component of the electric field (E_y) in MGSE, being a good approximation of the dawn-dusk electric field near midnight, is used. We also use differential flux data of energetic ion composition (including hydrogen, helium, and oxygen ions) and energetic electrons measured by RBSPICE and MagEIS, respectively.

To provide a more global context for this event, we also use the following space- and ground-based data sets. The space-based data are acquired from field and particle measurements at two spacecraft with small radial and/or azimuthal separation from RBSP: magnetic field vector data (3 s, Auster et al., 2008) from NASA's Time History of Events and Macroscale Interactions during Substorms (THEMIS) probe-A (Angelopoulos, 2008); and spin-averaged (~10 s) differential energetic electron and proton flux data from the Synchronous Orbit Particle Analyzer (SOPA) observations onboard one of the Los Alamos National Laboratory (LANL) geosynchronous satellite, LANL-04A (cf. Reeves, Belian, et al., 1996). The ground-based data are from ground magnetometers (1 min average) at several nightside middle-latitude stations, as described below.

3. Observations

3.1. Event Overview

We investigate a substorm event on 23 December 2016 that took place during a high-speed solar wind stream (HSS, ~700 km s^{-1}) and weak geomagnetic storm (minimum Dst = −40 nT). From 1800 to 1830 UT, four different spacecraft were closely spaced in the premidnight (2200–2300 MLT) inner magnetosphere, as shown in Figure 1a. The two Van Allen Probes (RBSP-A and -B) moved near their apogees ($r = 5.8\ R_E$) with a small azimuthal separation of ~0.5 R_E (corresponding to a local time separation of ~20 min). On the other hand, two other satellites, THEMIS-A and LANL-04A, were located at different radial distances. THEMIS-A

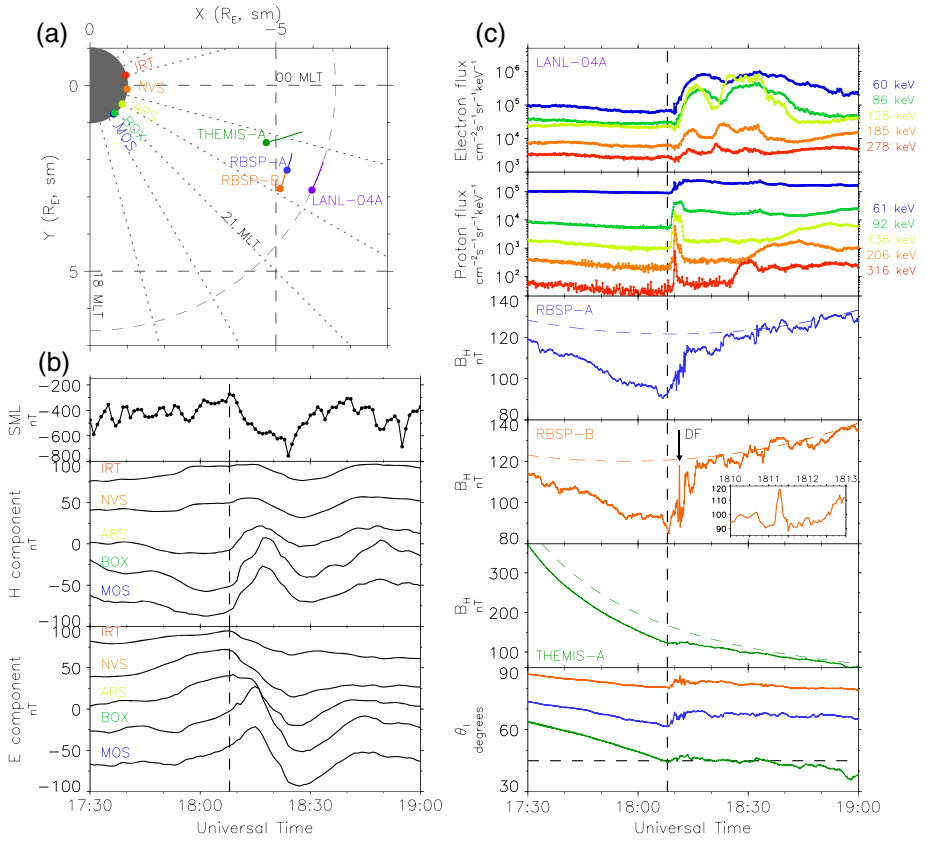

Figure 1. (a) Locations of the RBSP-A, RBSP-B, THEMIS-A, and LANL-04A spacecraft from 1800 to 1830 UT on 23 December 2016, together with five ground magnetometer stations at nightside middle latitudes (see text). (b) SML index and the H and E components at the five ground magnetometer stations during the interval of 1730–1900 UT. (c) Electron and proton fluxes at LANL-04A; the B_H component variations at RBSP-A (blue), RBSP-B (orange), and THEMIS-A (green); and the magnetic elevation angles measured by the three spacecraft for 1730–1900 UT. Dashed curves in the third to fifth panels represent the quiet time (Kp = 0) T89 model fields at RBSP-A, RBSP-B, and THEMIS-A. A zoomed-in view of a sharp dipolarization front (DF) signature at RBSP-B for 1810–1813 UT is also shown in the fourth panel. Vertical dashed line denotes substorm onset time (1808 UT) defined by SML index.

moved radially outward from $r = 5.0$ to 5.9 R_E near the 2300 MLT meridian, while LANL-04A moved from 2220 to 2250 MLT at GEO.

In order to characterize the geomagnetic substorm activity, Figure 1b presents the SuperMAG AL (SML) index (Gjerloev, 2012; Newell & Gjerloev, 2011) for the 1.5-hr interval of 1730–1900 UT on 23 December 2016, together with the *H* and *E* components of the ground magnetic field at five middle-latitude stations in the midnight sector: Irkutsk (IRT, geomagnetic latitude = 47.8°, MLT = UT + 6.90 hr), Novosibirsk (NVS, 51.3°, MLT = UT + 5.4 hr), Arti (ARS, 52.9°, MLT = UT + 3.8 hr), Borok (BOX, 54.5°, MLT = UT + 2.6 hr), and Moscow (MOS, 51.9°, MLT = UT + 2.5 hr).

A strong negative excursion of the SML index started at 1808 UT (dashed line), which is defined as the substorm onset in this study. After that, the SML index reached its minimum (about −800 nT) at 1824 UT, and then recovered rapidly. The SML variations reflect the intensity of westward auroral electrojet that developed as a result of substorm current system formation. Coincident with the developing westward electrojet, the five middle-latitude stations observed positive bays in the magnetic *H* component. The magnetic positive bays on the ground are usually interpreted in terms of the formation of substorm wedge-type FAC system, consisting of a pair of upward FAC at its eastern edge and downward FAC at its western edge (McPherron et al., 1973). Thus, the middle-latitude magnetometer data suggest that the wedge-type current system extended at least ~5 hr in MLT. On the other hand, the concurrent magnetic *E* component variations are often used to infer the central meridian of the wedge current because they are asymmetric with respect to the central meridian: i.e., a positive change at earlier local time than the central meridian and a negative

change at later local time. During the positive bay interval, the E component increased at BOX and MOS in the earlier local time sector than 2100 MLT, while it decreased at NVS and IRT in the later local time sector than 2300 MLT. At the in-between station, ARS (~2200 MLT), the E component remained almost unchanged for 5 min after the onset, and then decreased. Judging from these H and E component variations, it is suggested that the large-scale wedge current system extending ~5 hr in MLT was formed after the onset, centering around ARS.

Figure 1c shows observations of geosynchronous electron and proton injections at LANL-04A for the interval of 1730–1900 UT, together with local magnetic dipolarizations at RBSP-A, RBSP-B, and THEMIS-A inside GEO. From top to bottom, displayed are the energetic electron (60–280 keV) and proton (60–320 keV) fluxes at LANL-04A; the B_H components at the three spacecraft inside GEO; and the magnetic elevation angles, as defined by $\theta_I = \tan^{-1}(B_H/(B_V{}^2 + B_D{}^2)^{1/2}$. Here $\theta_I > 45°$ indicates that the spacecraft was in a B_H-dominant region closer to the magnetic equator. Dashed curve represents the B_H component of the model magnetic field, given by the Tsyganenko 1989 "T89" (Tsyganenko, 1989). Before the substorm onset, the θ_I value was >80° ($Z = -0.07\ R_E$ in solar magnetic, SM, coordinates) at RBSP-B, ~65° ($Z = -0.35\ R_E$) at RBSP-A, and ~45° ($Z = -0.85\ R_E$) at THEMIS-A. At the same time, LANL-04A was located at $Z = -0.45\ R_E$, which means that LANL-04A was slightly away from (closer to) the magnetic equator compared to RBSP-A and -B (THEMIS-A). These results ensure that the four spacecraft were continuously close to the magnetic equator throughout the event.

Approximately 2 min after the substorm onset, LANL-04A observed a gradual electron flux enhancement following a weak, short flux drop. The gradual electron flux enhancement had no significant energy dispersion, i.e., electron dispersionless injection. At the initial weak electron flux drop, on the other hand, the proton fluxes sharply increased over the range of 60–320 keV. In other words, the proton dispersionless injection onset preceded the electron dispersionless injection onset by about 1 min. The proton flux enhancement sustained a higher flux level in the two lowest energy channels, while it became a more transient signature (<4 min) in higher energy channels. The duration of the transient proton flux enhancement tended to be shorter with increasing energy. Such a proton flux signature may be explained by a combined effect of localized energization, rapid radial transport, and energy-dependent magnetic curvature/gradient drift. The electron and proton flux observations indicate that LANL-04A was positioned in the electron and proton injection regions. Two other LANL satellites, LANL-97A in the 1830–1900 MLT sector and LANL-02A in the 0245–0315 MLT sector, observed the energy-dispersed signatures of corresponding proton and electron injections, respectively (not shown here).

Before the geosynchronous injections, the magnetic field at RBSP-A and -B was stretching tailward, as identified by a gradually decreasing B_H with a slope of ~1 nT min^{-1}. Both probes observed a further negative excursion in the B_H component around the substorm onset, although the small negative B_H excursion started slightly earlier at RBSP-A (~1804:45 UT) than at RBSP-B (~1806:20 UT). Following the negative excursion, a strong, sustained local dipolarization was observed by both probes. Whereas the sustained local dipolarizations at RBSP-A and -B exhibited roughly similar evolution on the substorm timescale, their shorter-timescale B_H variations behaved differently: RBSP-B observed large B_H fluctuations at the early stage of dipolarization development, but no corresponding B_H fluctuations were seen at RBSP-A. Particularly, the first B_H enhancement at RBSP-B, which was initiated at ~1811 UT, was of the sharpest, shortest-lived (~25 s) nature with a peak-to-peak amplitude of ~25 nT. Such a transient B_H spike apparently resembles DFs: an earthward-propagating boundary which is formed on the leading edge of BBFs in the near-Earth tail and can separate BBF's plasma from the ambient plasma sheet (e.g., Nakamura et al., 2002; Runov et al., 2009). We call here simply the transient B_H spike "DF" in order to differentiate from the large-scale, sustained dipolarization in the inner magnetosphere. The justification of the use of the term "DF" is partly supported by the fact that the accompanying electric field and energetic particle changes had similarities to those associated with previously reported magnetotail DFs, which we will show later. The clear distinction between RBSP-A and -B suggests that the DF was highly localized around RBSP-B.

Before the substorm onset, on the other hand, THEMIS-A moved radially outward from $r = \sim 4\ R_E$ to $r = \sim 5\ R_E$. Due to the radially outward motion of the spacecraft, B_H at THEMIS-A decreased steeply from ~400 to ~100 nT. After the onset, THEMIS-A, which was located at $r = 5.3\ R_E$ around 2300 MLT, observed a local magnetic dipolarization but no corresponding DF.

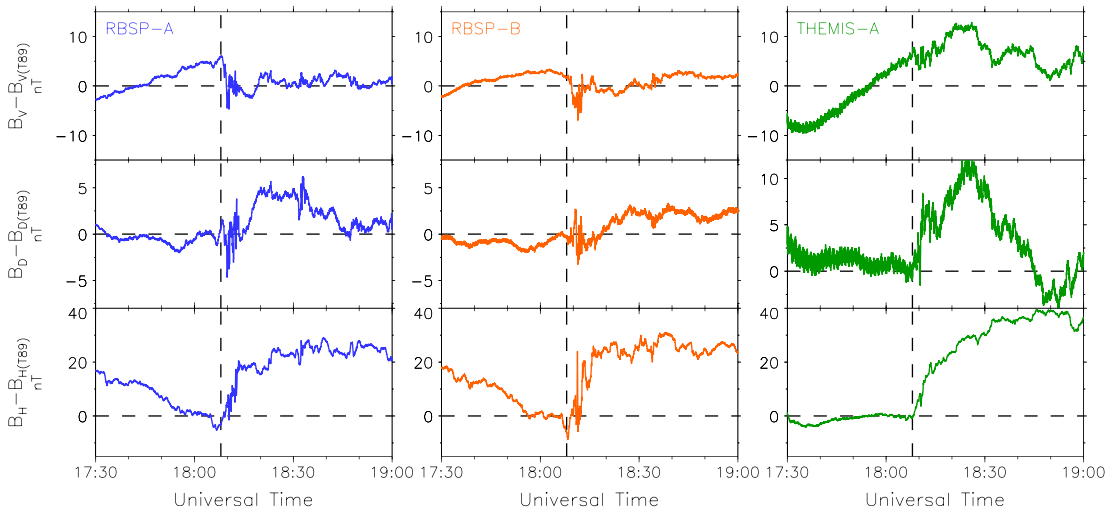

Figure 2. The three components of the residual magnetic field variations, B_V–$B_{V(T89)}$, B_D–$B_{D(T89)}$, and B_H–$B_{H(T89)}$, observed by RBSP-A (blue), RBSP-B (orange), and THEMIS-A (green) during 1730–1900 UT on 23 December 2016. $B_{(T89)}$ is the quiet time (Kp = 0) T89 model field. Vertical dashed line denotes the substorm onset time at 1808 UT.

3.2. Dipolarization Signatures Inside GEO

Figure 2 presents the three components of the residual magnetic field ($\Delta B_V = B_V$–$B_{V(T89)}$, $\Delta B_D = B_D$–$B_{D(T89)}$, and $\Delta B_H = B_H$–$B_{H(T89)}$) at RBSP-A, RBSP-B, and THEMIS-A during 1730–1900 UT, after subtracting the T89 model field from the observed field. At RBSP-A and -B, the ΔB_H component decreased before the onset, while ΔB_V increased. Such ΔB_H and ΔB_V changes indicate that the magnetic field was stretching into a more tail-like configuration. On the other hand, the ΔB_H decrease at THEMIS-A was little pronounced, while the ΔB_V increase was more significant than that at RBSP-A and -B. This is likely because THEMIS-A moved in the radially outward direction. After the substorm onset, the three satellites observed local magnetic dipolarizations, characterized by a large ΔB_H enhancement and ΔB_V depression.

The dipolarization-related B_D change is a good indicator to infer the location of a substorm wedge-like current system (Nagai, 1982). When a probe is located eastward (westward) of the central meridian of the wedge current system, B_D at the probe should undergo a negative (positive) excursion. RBSP-A and -B observed a large-scale negative excursion in B_D after the onset, although transient positive and negative enhancements were superimposed on the large-scale negative excursion. The amplitude of the negative excursion was relatively smaller at RBSP-B than at RBSP-A. The B_D variations suggest that both RBSP-A and RBSP-B were eastward of the central meridian of the wedge-like current system but RBSP-B was relatively closer to the central meridian. The central meridian is almost consistent with that inferred from the magnetic positive bays on the ground (Figure 1b).

Unlike the B_D excursion at the two RBSP spacecraft, a large positive excursion in B_D was detected at THEMIS-A that was located eastward of RBSP-A. However, the positive B_D excursion is inconsistent with that inferred from the region-1-sense wedge current system. One possible scenario is that the positive B_D excursion at THEMIS-A may be caused by the inner loop of double-loop wedge current system, i.e., the eastern upward FAC of the region-2-sense system which is paired with the original region-1-sense system in the outer region (Ohtani et al., 1990; Sergeev et al., 2014). If the region-2-sense upward FAC develops at a radial distance between THEMIS-A and RBSP-A/-B, THEMIS-A might detect positive changes in B_H and B_D, which are qualitatively consistent with our observations.

3.3. Injection Signatures Inside GEO

To understand how energetic particle injections were correlated with the concurrent local dipolarizations inside GEO, Figure 3 presents the RBSP-A (left panels) and -B (right panels) observations of spin-averaged differential fluxes of 30–470 keV electrons, and 54–270 keV hydrogen (H), 65–400 keV helium (He), and 140–400 keV oxygen (O) ions at 1730–1900 UT on 23 December 2016. During the local dipolarizations, RBSP-A and -B observed typical signatures of energetic electron and ion flux enhancements

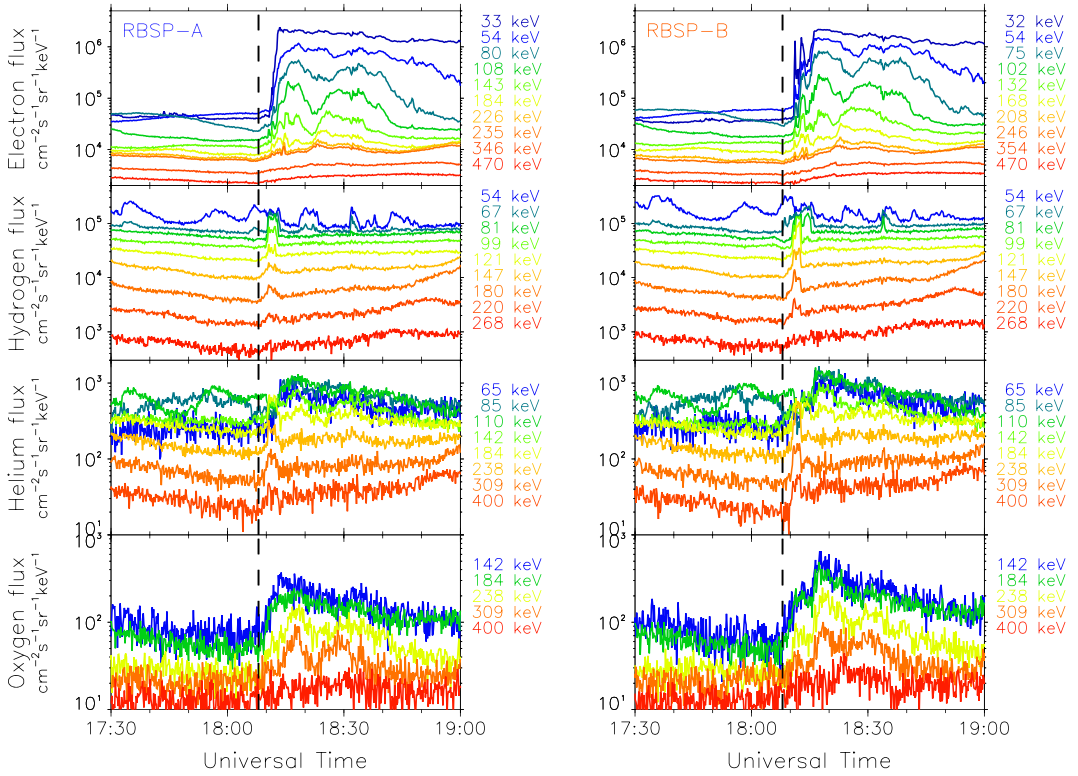

Figure 3. Spin-averaged fluxes of electrons and hydrogen, helium, and oxygen ions measured by RBSP-A (left) and -B (right) during 1730–1900 UT on 23 December 2016. Vertical dashed line represents the onset of substorm at 1808 UT.

(injections) inside GEO, as seen in the statistical results of Motoba et al. (2020). Whereas the large-scale injection signatures were roughly similar between the closely aligned RBSP-A and -B, the shorter-timescale variations and/or flux levels at the early stage of the injections were different between the two probes. The most noticeable difference is that the initially injected electrons exhibited a transient dispersionless signature at RBSP-B, but not at RBSP-A. The transient electron dispersionless injection at RBSP-B concurred exactly with the transient DF. Further details of their relationship will be demonstrated later. On the other hand, RBSP-A observed the corresponding electron injection signature, but it seemed to be energy-dispersed.

In contrast to the electron injections with distinctly different signatures, both RBSP-A and -B observed H ion flux enhancements almost simultaneously over the range from ~80 up to 220 keV, representing a dispersionless character. When taking a close look at the H ion injection signatures, however, it is noticeable that the higher-energy H ion flux enhancements became sharper and stronger at RBSP-B than RBSP-A. Such different H ion injection signatures could be associated with the presence or absence of the concurrent transient DF. The H ion fluxes dropped within about 5 min, and then they were followed by a recovery toward preonset flux levels. A similar transient flux enhancement can also be seen in the He ion fluxes at >180 keV, but the upper threshold energy of the He ion injections (~600 keV) is at least twice higher than that of the H ion injections. On the other hand, the lower-energy (<150 keV) He ion fluxes underwent a gradual rise and subsequent gradual decay. Unlike the H and He ion injections, the O ion injections were much more gradual. Indeed, the O ion flux enhancement reached a peak after 1815 UT. The O ion injections had no/little apparent difference between RBSP-A and -B at the initial stage (before 1815 UT), but at the late stage (after 1815 UT) the intensity of the sustained O ion flux enhancement was slightly stronger at RBSP-B than at RBSP-A.

3.4. Radial Evolution of Injections

In this section we investigate how differently energetic particles behave not only between RBSP-A and -B but also between LANL-04A and RBSP-A/-B, with a focus on the early stage of the injections of interest. Figure 4 displays spin-averaged fluxes of electrons (left panels) and H ions (right panels) in the 10 different energy

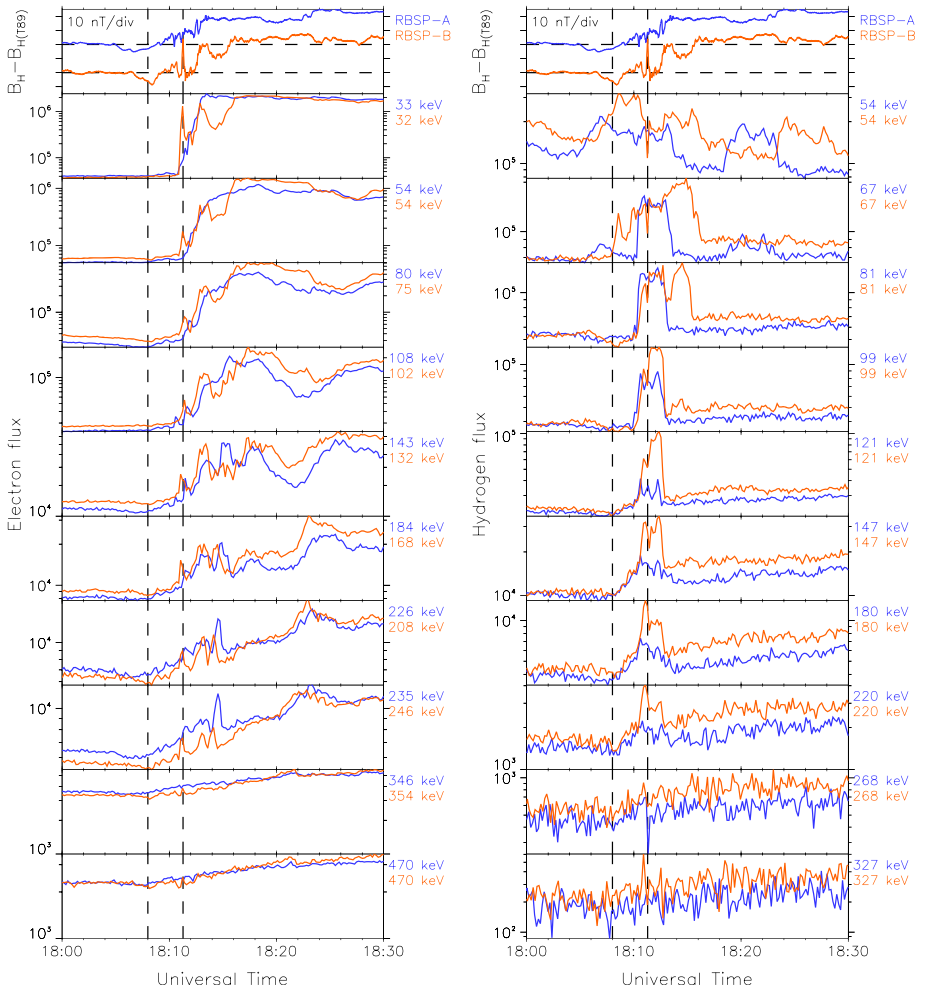

Figure 4. Spin-averaged electron (left) and hydrogen ion (right) fluxes at 10 different energy channels, observed by RBSP-A (blue) and -B (orange) for 1800–1830 UT. The B_H variations at both probes are shown in the top panel. The first and second vertical dashed lines denote the substorm onset time (1808 UT) and DF peak time (1811:17 UT) at RBSP-B, respectively.

channels of 30–470 keV observed at RBSP-A and -B for the interval of 1800–1830 UT, together with their ΔB_H component variations in the top panel. The first and second vertical dashed lines indicate the ground substorm onset time (1808 UT) and DF peak time (1811:17 UT).

At the initial stage of the large-scale electron injection, there were some shorter-timescale flux enhancements which behaved differently between RBSP-A and -B. It is clear that the first electron flux enhancements at RBSP-B appeared as a dispersionless, short-timescale injection pulse which occurred concurrently with the transient DF. The electron dispersionless injection had the most significant flux enhancement at 32 keV and its signature became less clear at $\geq \sim 350$ keV. On the other hand, RBSP-A observed the corresponding electron flux enhancements in the same energy range, but the electron flux enhancements represented an energy dispersion, i.e., a dispersed injection. Indeed, the initial electron injection pulses at RBSP-A lagged them at RBSP-B by ~20–25 s at $\geq \sim 75$ keV (~45 s at 30–55 keV). Such dispersion signals likely arise from the energy-dependent electron drift velocities after electrons are injected simultaneously from an injection region. The different electron injection signatures between RBSP-A and -B allow us to conclude that the RBSP-B location was inside the electron injection region, while the RBSP-A location was slightly eastward away from the injection region. Based on the time lag and azimuthal distance between RBSP-A and -B, we estimated the energy-dependent eastward propagation speeds to be 125–160 km s^{-1} at $\geq \sim 75$ keV and 70 km s^{-1} at 30–55 keV. Such propagation speeds are roughly consistent with those inferred from the energy-dependent magnetic curvature/gradient drifts.

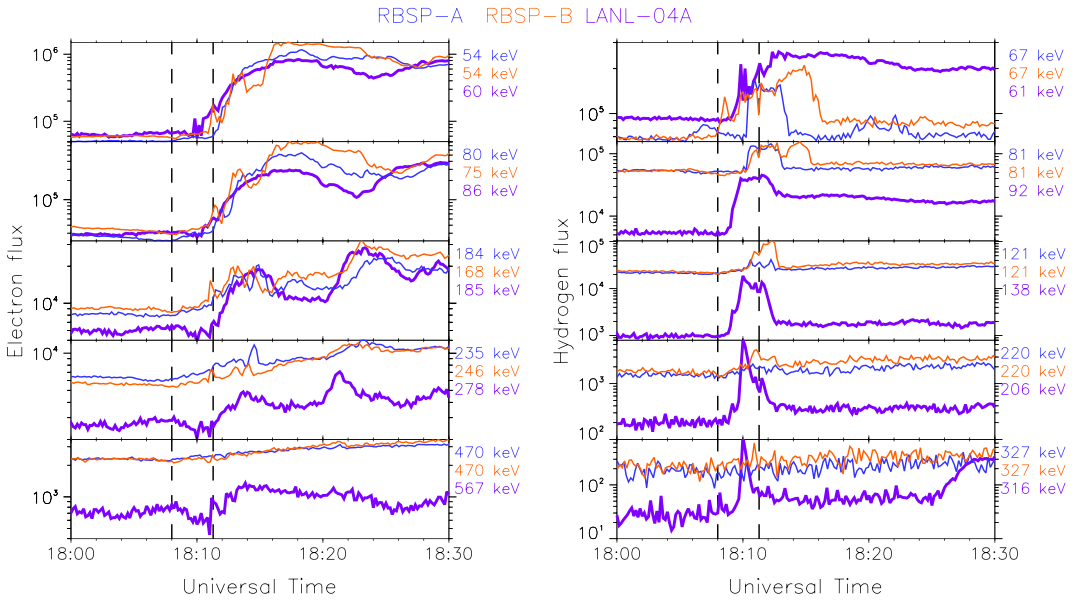

Figure 5. Electron and hydrogen ion fluxes at five different energy channels, observed by RBSP-A (blue), RBSP-B (orange), and LANL-04A (purple) for 1800–1830 UT. The first and second vertical dashed lines are the same as those in Figure 4.

In contrast to the electron injection signature, the H ion injection represents a more transient, shorter-lived nature, particularly at 99–220 keV. Both RBSP-A and -B observed the H ion flux enhancements to start at ~1 min before the DF onset and persist for ~3 min following the onset. The flux intensity was elevated by factors of 2 up to 10, depending on the energy. In addition to such common features between RBSP-A and -B, the local presence or absence of the sharp DF seemed to lead to two main differences in the H ion dispersionless injection signature between RBSP-A and -B. One difference is that the intensity of the H ion flux enhancement was much higher at RBSP-B than RBSP-A. Another is that at the DF peak the H ion flux at RBSP-B experienced a sudden drop embedded within the H ion injection, while no corresponding flux drop was seen at RBSP-A. Such a transient H ion flux depression at RBSP-B became much more pronounced (sharper) in lower-energy channels. The H ion flux depression associated with rapidly increasing magnetic field could be understood as a diamagnetic nature.

Figure 5 displays comparison of local energetic particle injections at LANL-04A and RBSP-A/-B to examine the radial development of the injections transported earthward from 6.6 to 5.8 R_E. For the comparison, we used the five nearest energy channels of RBSP-A/-B and LANL-04A. Overall, the large-scale evolution of <200 keV electron injections at LANL-04A resembled that at RBSP-A and -B in terms of the temporal variations and flux levels, although there were some differences in the short-timescale variations. The arrival time of the initial electron flux enhancement at LANL-04A was ~1810 UT, preceding that at RBSP-A/-B by ~1 min. Given that the delay between the electron injection arrival times at 5.8 and 6.6 R_E results from the earthward transport of injected electrons, the earthward propagation speed is estimated to be ~85 km s^{-1}. On the other hand, the >200 keV electron flux levels were dramatically different between RBSP-A/-B and LANL-04A. This is likely because higher energy electrons that are injected at GEO are filtered out of the deeper electron injections inside GEO due to magnetic curvature/gradient drift.

As mentioned above, the arrival of the geosynchronous ion injection preceded that of the geosynchronous electron injection by ~1 min and the ion injection had a sharper dispersionless character than the electron injection. The ion dispersionless injection became more transient with increasing energy and its upper threshold energy was ~500 keV (not shown). A similar ion dispersionless injection signature was detectable at both RBSP-A and -B. At > ~ 80 keV, the onset of the initial ion flux enhancement at RBSP-A/-B lagged that at LANL-04A by ~1 min. The time lag is consistent with that for the electron injection. This result indicates that energetic particles were radially transported at a species-independent propagation speed of ~85 km s^{-1}. At RBSP-A (-B), little or no clear transient ion flux enhancement was seen in energy channels above 220 keV

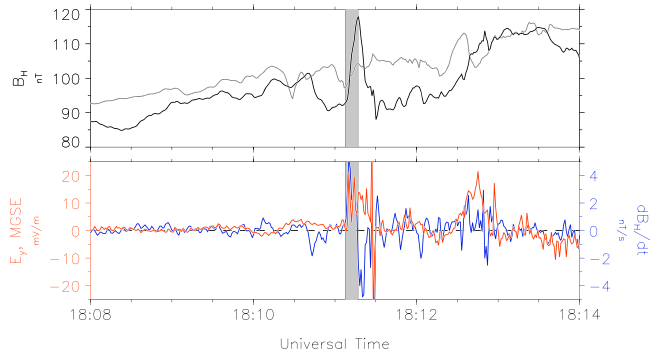

Figure 6. The top panel shows the B_H component of the magnetic field at RBSP-B (black) and RBSP-A (gray) from 1808 to 1814 UT on 23 December 2016. The bottom panel indicates the E_y component of the electric field (red) and the time derivative of B_H (blue: dB_H/dt). The DF interval is shaded in light gray.

(269 keV), which is about half of the upper threshold energy at LANL-04A. The different upper threshold energies at LANL-04A and RBSP-A/-B could be explained in terms of energy-dependent magnetic curvature/gradient drift. In other words, the higher energy ions should undergo the strong westward drift before they reach the RBSP site.

3.5. Properties of DF-Related Fields

Figure 6 presents the B_H component and E_y component at RBSP-B for the interval of 1808–1814 UT, in order to characterize the short-lived DF-related fields that impacted energetic particles. In the top panel, the B_H component at RBSP-A (gray) is overplotted just for comparison. At the early stage of the large-scale dipolarizations at both probes, only RBSP-B observed the transient DF, of which B_H began to abruptly jump at 1811:10 UT and reached its maximum at 1811:17 UT. The DF had a peak-to-peak amplitude of ~25 nT in B_H. After that, the B_H amplitude returned to the pre-DF levels within ~12 s after the DF peak. The DF was preceded by a short-duration (~30 s) negative dip in B_H (often called "DF-dip").

The bottom panel of Figure 6 displays 1-s averages of the E_y component (red curve) in MGSE coordinates observed by RBSP-B. E_y increased sharply up to ~20 mV m^{-1} at the DF. Such a strong E_y enhancement can be a mixture of the inductive and convection fields, although it is impossible to distinguish explicitly the relative contribution of each component. Inductive electric fields during dipolarizations/DFs are suggested to be an important driver for local nonadiabatic energization of preexisting oxygen ions in the inner magnetosphere when the temporal/spatial scale is comparable to the oxygen gyroperiod/gyroradius (Keika et al., 2013, and references therein). One possible way to assess the inductive effect qualitatively is to compare with the time derivative of B_H ($\delta B_H/\delta t$: blue curve) as a proxy (Ohtani et al., 2010). Although there are exceptions, both E_y and $\delta B_H/\delta t$ enhancements are roughly correlated, particularly at $\delta B_H/\delta t > 0$. This suggests that the inductive component was more or less effective at the transient DF.

The impulsive, westward E_y enhancement at the DF is also responsible for the rapid earthward $\mathbf{E} \times \mathbf{B}$ drift, being up to ~180 km s^{-1} in maximum and ~100 km s^{-1} on average. The earthward collapse of the DF fields can transport energetic particles into GEO or even closer to Earth. Indeed, the average $\mathbf{E} \times \mathbf{B}$ drift speed is almost comparable to the radial propagation speed (~85 km s^{-1}) of energetic electrons and ions injected from GEO to 5.8 R_E. The radial propagation speed is faster than the average speeds of injections (~24 km s^{-1}, Reeves, Friedel, et al., 1996) and dipolarizations (~50 km s^{-1}, Ohtani et al., 2018) inside GEO. Using the propagation speed (~100 km s^{-1}) and duration (7 s) of the DF, the DF thickness is estimated to be ~700 km, comparable to a scale of a few ion gyroradii. These properties of the DF-related fields inside GEO are very similar to those of typical DFs, usually embedded in BBFs in the Earth's magnetotail (e.g., Nakamura et al., 2002; Runov et al., 2009; Sergeev et al., 2009).

Following the short-lived DF, RBSP-B observed a relatively longer-lived B_H enhancement. Whereas the positive B_H slope was more gradual than that of the DF, the accompanying positive E_y spike had almost the same timescale and amplitude as the DF-related E_y spike. If the E_y spike at $\delta B_H/\delta t > 0$ is inductive, the E_y spike should be much sharper and stronger at the DF than at the following gradual B_H enhancement. Indeed, such a sharper and stronger E_y spike is recognizable within the first 10 s of the DF by using the 32-Hz sampling EFW data (not shown here), rather than the presented 1-s average data.

3.6. DF Effects on Energetic Particles

Let us here turn back to electron and H ion flux changes at RBSP-B, with more focus on the pitch angle distributions (PADs) of energetic particles in response to the DF. As the DF was of an extremely transient nature, we analyzed the electron and H ion PADs using the "unbinned" MagEIS and RBSPICE Level 3 data with a time resolution of sector samples per spin. For this analysis, we removed the RBSPICE data in which the Poisson statistical percent error was larger than 50% (for more details on the error, see the RBSPICE Science Data Handbook at http://rbspice.ftecs.com/Data). Figures 7a and 7b, respectively, show the B_H variations

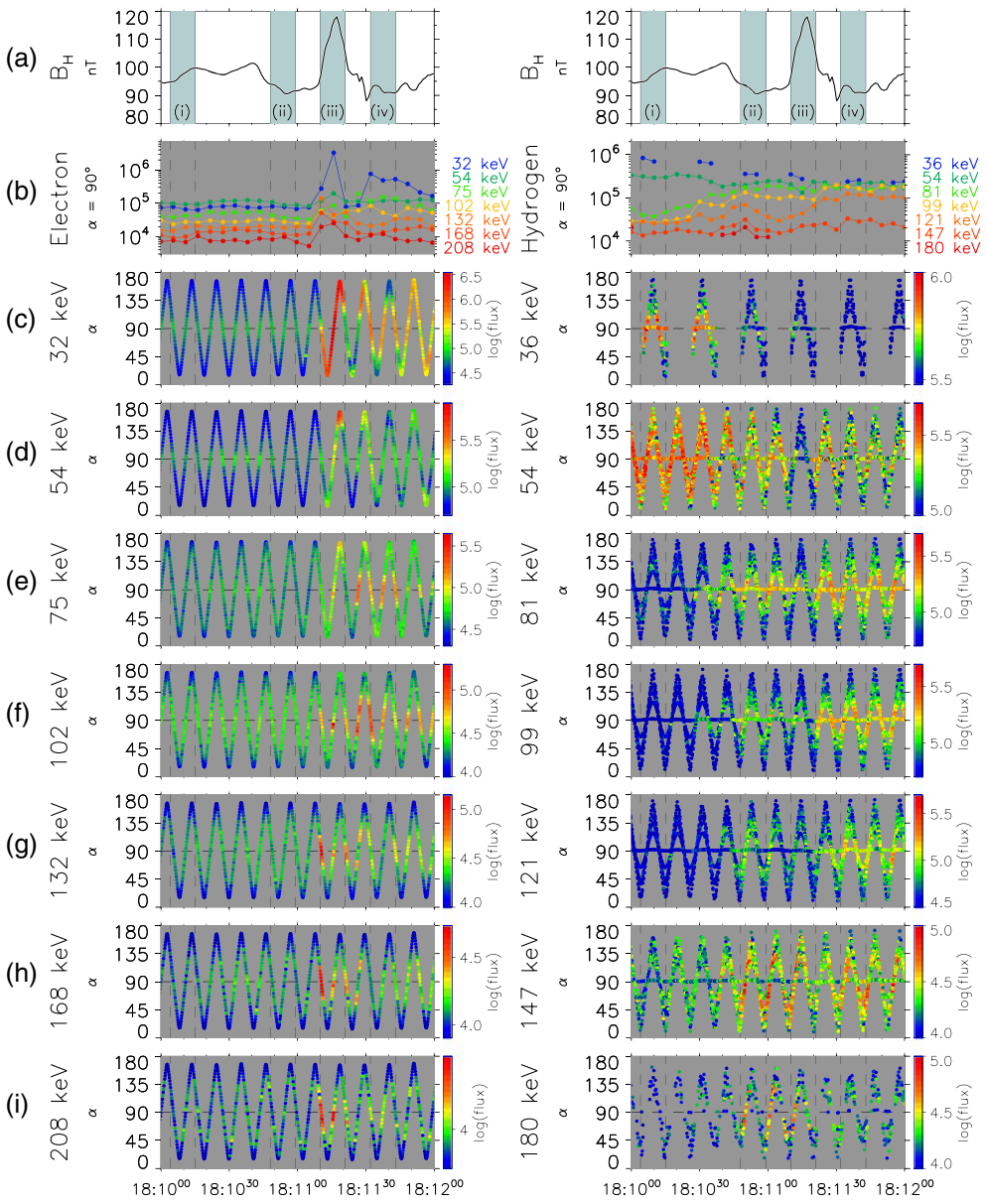

Figure 7. (a) B_H, (b) electron and hydrogen ion fluxes at α = 90°, and (c–i) electron and hydrogen ion PADs at seven different energy channels observed at RBSP-B for the 2-min interval of 1810–1812 UT.

and stacked plots of electron (left) and H ion (right) flux data at local pitch angle (α) = 90° for the 2-min interval of 1810–1812 UT around the DF. For the stacked H ion flux plots, we used only the H ion flux data at times when the five RBSPICE telescopes 1–5 other than the telescope 0 looked at α = ~90°. Figures 7c–7i present electron and H ion PADs in the seven different energy channels.

The 34–208 keV electron fluxes at α = 90° began to increase simultaneously at the DF onset. However, a close look at the DF-related electron flux peaks in Figure 7b represents a small but identifiable time difference (~5 s) between higher- and lower-energy channels: the higher-energy (>130 keV) electron flux enhancement peaked at the DF arrival, while the lower-energy (<75 keV) electron flux peak took place at the DF peak time. After the DF peak, the lower-energy electron flux decreased steeply. As seen in Figures 7c and 7d, the lower-energy (32–54 keV) electron fluxes were quasi-isotropically enhanced during the DF. On the other hand, it is clear from Figures 7g and 7h that the higher-energy electron flux enhancements were most significant around α = 90° at the DF onset, but less pronounced at the other pitch angles. These results suggest that the injected electrons were trapped and accelerated by the earthward-penetrating

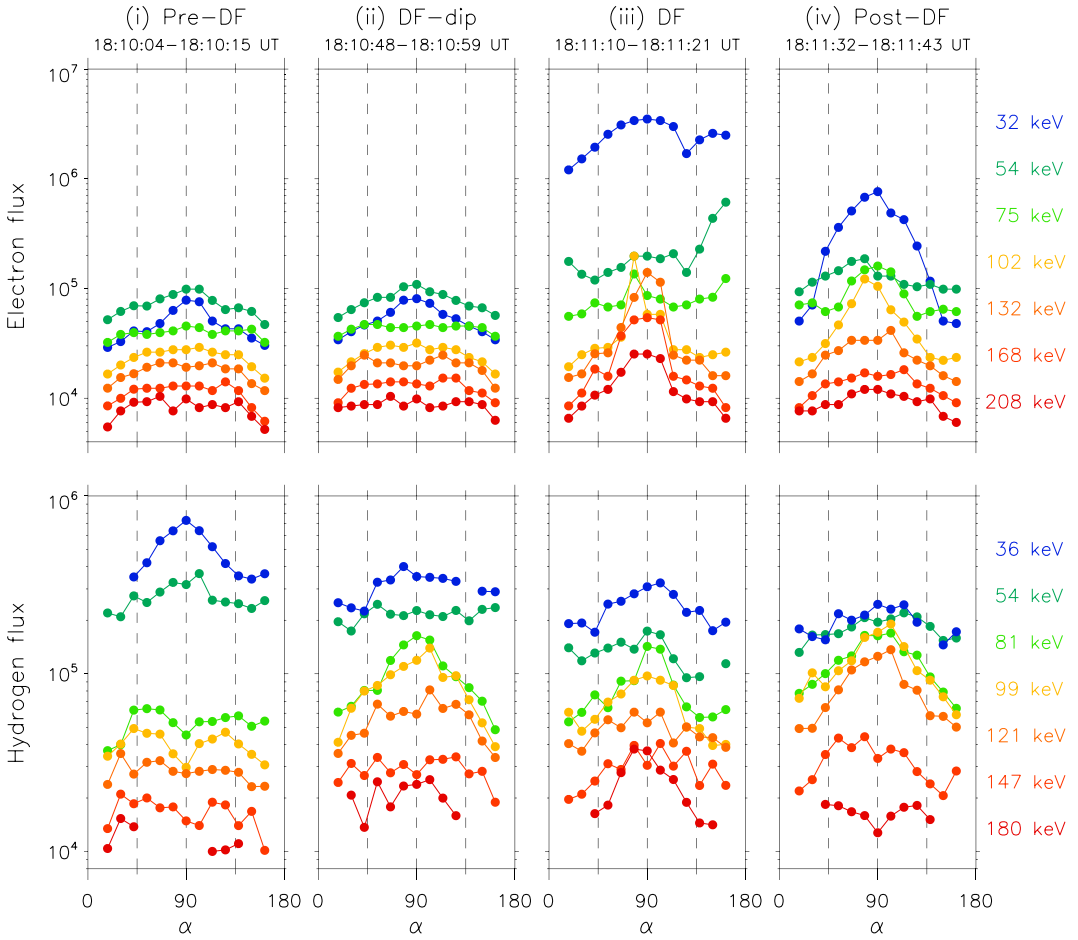

Figure 8. Electron and hydrogen ion PADs at four different time intervals (i), (ii), (iii), and (iv) around the DF at RBSP-B, shown in the top panel of Figure 7.

DF, but the higher-energy electrons drifted away from the localized DF region inside GEO where the magnetic curvature/gradient drift was a strong effect.

Compared to such remarkable electron flux enhancements on the DF time scale, the DF-related H ion flux changes were relatively less pronounced. During the interval 1810–1802 UT, there is a general tendency for the ≤54 keV (≥81 keV) H ion fluxes at $\alpha = 90°$ to decrease (increase) gradually. The H ion fluxes at 54 keV underwent a further transient depression at the DF. Such a sudden transient flux depression can be seen at all pitch angles (see Figure 7d). The higher-energy (≥81 keV) H ion fluxes at $\alpha = 90°$, on the other hand, exhibited two peaks: the first and second peaks appeared around the DF-dip (~1810:50 UT) and a B_H minimum (~1811:30 UT) just after the DF, respectively. Overall, the short-timescale H ion flux variations at ≥81 keV seemed to be in approximately antiphase with the B_H variations.

Figure 8 displays one-spin (~11 s) averaged PADs of electrons and H ions for the four different time intervals of (i) pre-DF, (ii) DF-dip, (iii) DF, and (iv) post-DF, as shown in Figure 7. The electron PADs for both (i) and (ii) represented a gradual pancake shape (peaked at 90°) at 32–54 keV and a flat-top shape (approximately equal flux at most pitch angles) at ≥75 keV. For (iii), the 32 keV electron fluxes at all pitch angles increased dramatically by more than one order of magnitude. Such an isotropic electron flux enhancement result in a flat-top-like PAD. As mentioned above, on the other hand, the >100 keV electrons had an extreme pancake-type PAD (i.e., a significant flux enhancement only around $\alpha = 90°$), which results likely from local betatron acceleration at the earthward-propagating DF. For (iv), the 32–54 keV electron fluxes dropped sharply, particularly at $\alpha = 0°$ and 180°. The resulting electron PADs exhibited a pancake shape with higher flux levels than the pre-DF. The ≥168 keV electron PADs quickly returned to a flat-top-like shape, like those at the pre-DF.

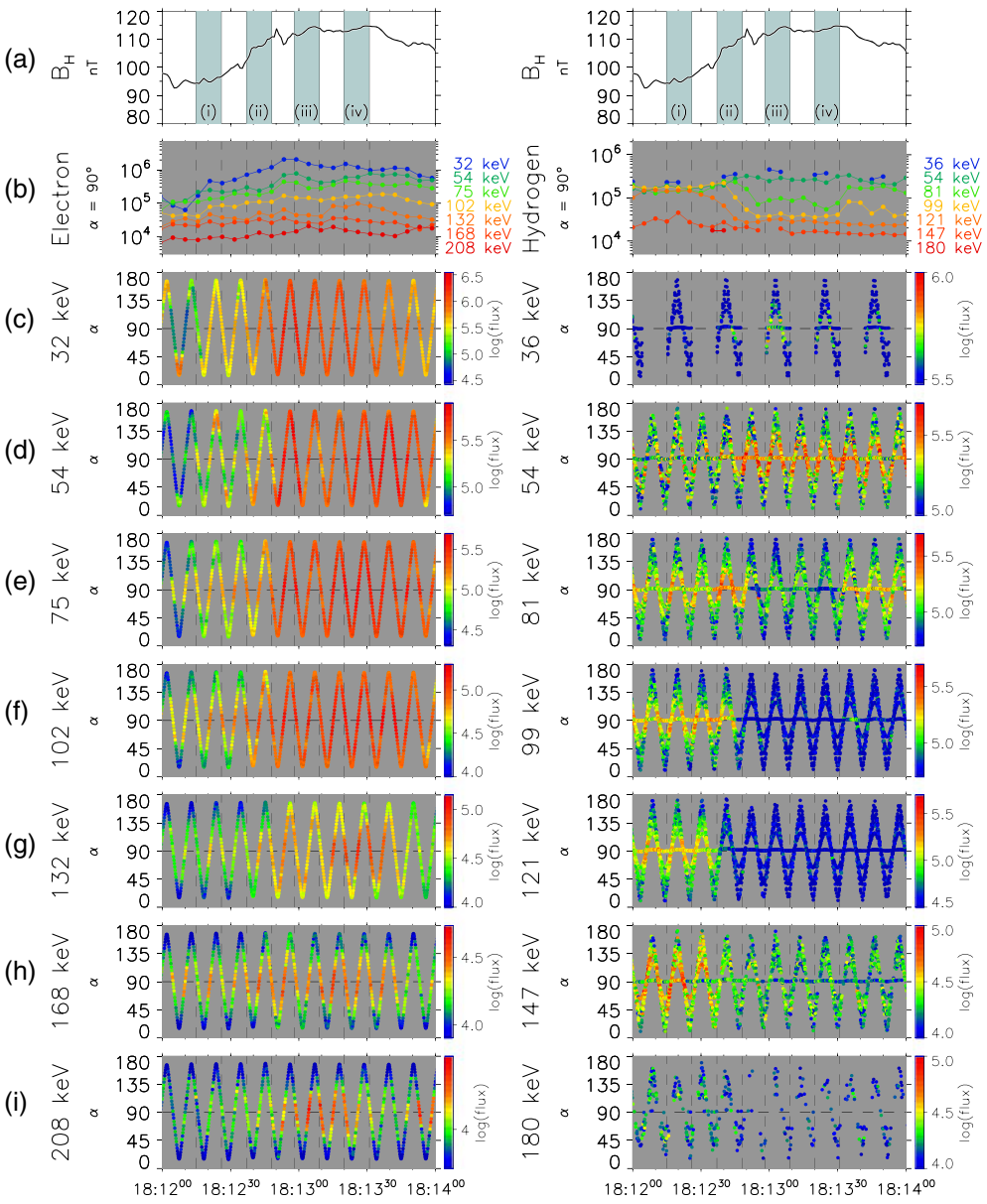

Figure 9. Same as Figure 7 but for the 2-min interval of 1812–1814 UT.

On the other hand, the H ion PADs for (i) were pancake-shaped at ≤54 keV and butterfly-shaped (peaked at 45° and 135°) at ≥81 keV. For (ii), in contrast to the electron PADs, the H ion PADs changed dramatically: the H ion fluxes at ≤54 keV exhibited a flat-top-like PAD resulting from a significant depression around $\alpha = 90°$, while the H ion fluxes at 81–121 keV had a pancake PAD with a significant enhancement around $\alpha = 90°$. For (iii), the higher-energy (≥147 keV) H ion fluxes increased around $\alpha = 90°$, resulting in a pancake PAD. In contrast, the ≤99 keV H ion fluxes decreased, presumably reflecting a local plasma pressure depression at the DF. For (iv) when B_H decreased again, the H ion PADs became a pancake shape at 81–121 keV and a flat-top-like shape at ≤54 keV, similar to those at the DF-dip for (ii). Particularly, the 99–121 keV H ions around $\alpha = 90°$ were most significantly enhanced in response to the B_H depression.

One may wonder whether the DF-related energetic particle behaviors are exceptional. To address the question we compare them with the response of energetic particles to subsequent relatively gradual B_H enhancement which started to increase at ~1812:15 UT. Figures 9 and 10 are, respectively, in the same formats as

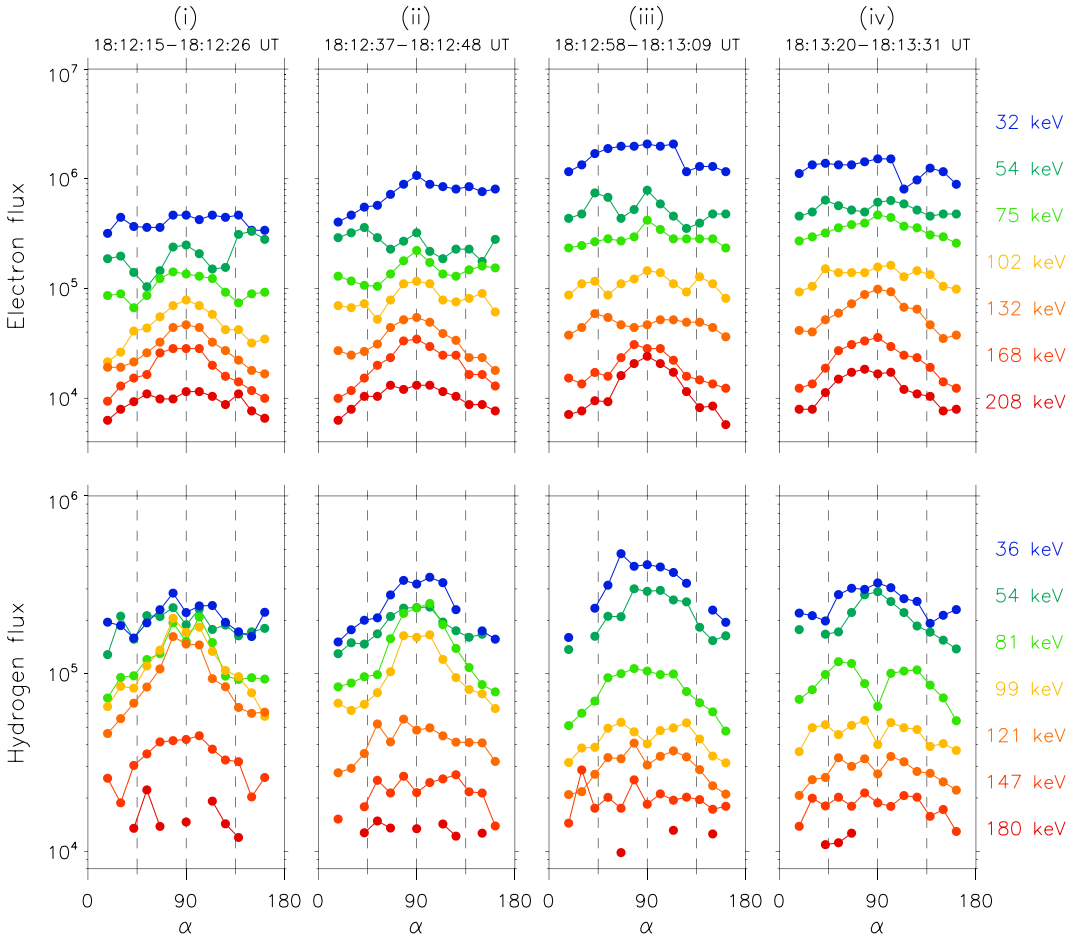

Figure 10. Same as Figure 8 but for the four different time intervals (i), (ii), (iii), and (iv) shown in the top panel of Figure 9.

Figures 7 and 8, but display the pitch angle dependent responses of energetic electron and H ion fluxes to the gradual B_H enhancement observed by RBSP-B at 1812–1814 UT.

From these comparisons, it is clear that the electron and H ion injection properties have many commonalities between the transient DF and subsequent gradual B_H enhancement: (1) the electron flux enhancement followed the gradual B_H enhancement (Figures 9a–9b); (2) the electron flux enhancement was almost isotropic at ≤102 keV, while at ≥132 keV it was mostly confined around $\alpha = 90°$ (Figures 9c–9i); (3) the energetic H ion fluxes at 81–147 keV varied in almost antiphase with B_H (Figures 9a–9b); and (4) the H ion flux enhancement preceded the electron flux enhancement by ~1 min. On the other hand, some differences existed in the PAD properties: (1) the 54 and 75 keV electron fluxes were more strongly elevated for the gradual B_H enhancement than for the DF; and (2) the electron fluxes at ≥100 keV was much stronger perpendicular anisotropy for the DF than for the gradual B_H enhancement. We suggest that such differences are caused by the different sharpness and/or timescale of B_H enhancement that could influence the degree of particle acceleration and/or transport.

4. Discussion

The principal results from this study include the following:

1. Substorm particle injections and local dipolarizations were observed by four closely located spacecraft at and inside GEO near the central meridian (~22 MLT) of an initially formed current wedge system. Their large-scale evolution was almost identical between the two RBSP spacecraft at ~0.5 R_E apart in the azimuthal direction.

2. In contrast, a distinctly different signature was found in the first injections at the two RBSP spacecraft: RBSP-B, located closest to the onset meridian, observed a dispersionless injection which occurred concurrently with a transient DF (timescale of ~25 s, peak-to-peak amplitude of ~25 nT), while RBSP-A, located slightly eastward from RBSP-B, observed a dispersed electron injection and a weaker dispersionless H ion injection with no corresponding DF.
3. The radial propagation speed of the injections from the LANL-04A to RBSP location was ~85 km s^{-1}, in good agreement with the average speed of the $\mathbf{E} \times \mathbf{B}$ earthward drift by the DF-related fields.
4. The transient DF fields significantly affect the energy- and pitch angle-dependent flux changes of the electrons and the H and He ions inside GEO. In contrast, the heavier O ions were much less affected by the DF fields.

Critical for this study were the limited spatial separations of the well-instrumented spacecraft. The LANL-04A and RBSP-A/-B satellites had a small radial separation of ~0.8 R_E in the same MLT meridian, while the RBSP-A and -B satellites were azimuthally separated by only ~0.5 R_E (20 min in MLT) at the same radial distance. Based on the time delay between the injection arrivals at and inside GEO, the radial propagation speed of the injection region was estimated to be ~85 km s^{-1}. This injection propagation speed was approximately equal to the average speed (~100 km s^{-1}) of the transient earthward $\mathbf{E} \times \mathbf{B}$ drift estimated from the DF-related fields at RBSP-B.

However, the determined earthward propagation in this study is relatively fast compared to some prior reports by two radially separated spacecraft at and inside GEO. For instance, Moore et al. (1981), using data from the ATS-6 and SCATHA satellites, reported that the hot plasma propagates earthward in close association with an equally abrupt magnetic field increase at velocities in the range of 10–100 km s^{-1}. Based on the CRRES–LANL satellite pair within $\pm$1 hr of local time, Reeves, Friedel, et al. (1996) reported that essentially all injection cases (nine events) were consistent with an earthward propagation of the substorm injection region, with an average earthward propagation speed inside GEO of ~24 km s^{-1}. Ohtani et al. (2018) found, although not for the injection region, that the dipolarization region inside GEO expands earthward at a finite speed of 50 km s^{-1}. The event studied here occurred under an HSS-driven magnetic storm condition. Therefore, it would be reasonable to speculate that the flow-breaking region during this substorm event was much closer to the Earth than that under nonstorm conditions. As a result, the DF and its accompanying injection region might be able to reach further inside GEO without significant deceleration.

The azimuthal scale of the penetrating injection region is important for understanding the dynamics of the process. In this study with the two closely spaced RBSP spacecraft, the measurements suggest that RBSP-B was in the core injection region in which local acceleration and/or rapid transport could be caused by the sharp DF, while RBSP-A was outside the core region. With no spacecraft measurements to the west of RBSP-B, however, we cannot conclusively determine how far in MLT the westward edge of the core region was extended. Typical special scale of DFs (or BBFs) in the near-Earth tail is 2–3 R_E (Nakamura et al., 2004; Runov et al., 2011). Given that the DF (injection region) has the same azimuthal scale and its eastern edge is the RBSP-B location, the westward edge might extend up to ~20 MLT meridian, roughly corresponding to the westward edge of the initial substorm current wedge.

It is interesting to note that, whereas the initial electron injection at RBSP-A was dispersed, the H ion injection represented a dispersionless signature but had a weaker flux enhancement than that at RBSP-B. This suggests that the eastward edge of the ion injection region extended to the RBSP-A location, unlike that of the electron injection region. This picture is not consistent with the conventional picture of electron and ion dispersionless injection boundaries, which are in the midnight to dawn MLT sector and in the dusk to midnight MLT sector, respectively (Birn et al., 1997b). Our measurements imply that both electron and ion injection regions are highly localized, but that they have different spatial extends with respect to the accompanying DF.

The transient DF impacts on energetic particle population inside GEO depended on species. As shown in Figure 4, the RBSP A-B comparison demonstrates that the local presence or absence of the penetrating DF determines whether the concurrent electron injection is a dispersionless or energy-dispersed signature. This is consistent with previous magnetotail observations of DFs (Gabrielse et al., 2014). Contrary to the electron injections, the H ion flux enhancements (i.e., injections) at >81 keV represented a dispersionless signature at both spacecraft, although the flux intensity was much stronger in the presence of the DF than

without, particularly for energies >100 keV. An interesting feature is that the DF was accompanied by a transient depression in the energetic H ion fluxes, rather than their enhancement. The H ion flux depression could be explained as the diamagnetic nature of plasma pressure by the sharp DF (B_H enhancement).

Like the H ion injection, the He ion injection also represents a transient dispersionless signature; its flux intensity is much stronger at RBSP-B than at RBSP-A. This suggests that the dynamics of He ions inside GEO are also affected by the transient DF-related fields. In contrast to such lighter ion species, the heavier ions exhibited a more gradual flux enhancement. In contrast to these lighter ion species, the heavier O ions exhibited a more gradual flux enhancement. An O ion flux enhancement is usually considered to be caused by local acceleration in the inner magnetosphere, or by adiabatic heating through the impulsive earthward transport of source population in the near-Earth plasma sheet. The local O ion gyroperiod at the RBSP location is ~10 s, which is slightly longer than (or comparable to) the timescale of the DF-related electric field. Therefore, one may expect that preexisting O ions at the RBSP location would experience a DF-induced nonadiabatic local acceleration and that the resulting O ion flux enhancement would be stronger for the with-DF case than the without-DF. Contrary to the expectation, however, the closely aligned RBSP observations indicated no/little significant differences in the O ion flux enhancement between the with-DF and without-DF cases. This result therefore implies that the transient DF-related fields have no significant effect on the local acceleration of O ions inside GEO, even though the DF timescale is shorter than (or comparable to) the O gyroperiod.

5. Conclusions

In conclusion, by examining fields and energetic particles data from four closely located satellites (RBSP-A, RBSP-B, LANL-04A, and THEMIS-A) we found that electron and ion dispersionless injections inside GEO were accompanied by a spatiotemporally localized DF. This DF occurred at the beginning stage of a sustained local dipolarization near the central meridian of a wedge-like current system formed immediately after the substorm expansion onset. The DF-related particle flux changes inside GEO at this epoch exhibited strong species-, energy-, and pitch angle-dependent features. This multispacecraft study clearly demonstrates that the electron and ion dispersionless injection regions inside GEO are well correlated with a highly localized DF that penetrates deeper in the inner magnetosphere. Future multispacecraft studies will be required to examine the spatial occurrence patterns of dispersionless injections inside GEO and the factors controlling their occurrence. In addition, the magnetic and electric field changes associated with such dispersionless injections will need to be examined to identify the operative physics processes at these times.

Acknowledgments

Work at JHU/APL was supported by National Aeronautics and Space Administration (NASA) grants 80NSSC19K0847, 80NSSC20K0699, NNX16AF74G, and JHU/APL Subcontract 937836 to the New Jersey Institute of Technology under NASA Prime Contract NAS5-01072, and by National Science Foundation (NSF) grant 1603028. Work at The Aerospace Corporation was supported by RBSP-ECT funding provided by JHU/APL Contract 967399 under NASA's Prime Contract NAS501072. T. M. is thankful to D. L. Turner for fruitful comment on the MagEIS data. The authors are grateful to the entire Van Allen Probes team for the use of Van Allen Probes data for this study. Specifically, we thank the following PIs: C. A. Kletzing for EMFISIS, J. R. Wygant for EFW, L. J. Lanzerotti for RBSPICE, and J. B. Blake for MagEIS. We would also like to acknowledge NASA Contract NAS5-02099 (PI: V. Angelopoulos) and K. H. Glassmeier, U. Auster, and W. Baumjohann for use of the THEMIS FGM data.

Data Availability Statement

Data from Van Allen Probes used in this study are available at CDAWeb (https://omniweb.gsfc.nasa.gov) and also at the individual instrument websites as follows: EMFISIS (https://em!sis.physics.uiowa.edu/data/index); EFW (http://www.space.umn.edu/rbspefw!data/); RBSPICE (http://rbspice.ftecs.com/Data.html); and MagEIS (https://www.rbsp!ect.lanl.gov/science/DataDirectories.php). SuperMAG indices and magnetometer data are available at the SuperMAG website (http://supermag.jhuapl.edu/) maintained by J. W. Gjerloev and the SuperMAG team with support from NSF in international collaboration with many organizations and institutes. THEMIS-A FGM data are available at the THEMIS Mission website (http://themis.ssl.berkeley.edu). LANL!04A SOPA data, although available by request to G. D. Reeves and M. G. Henderson at Los Alamos, are archived online (10.6084/m9.figshare.12292775).

References

Angelopoulos, V. (2008). The THEMIS mission. *Space Science Reviews*, *141*(1–4), 5–34. https://doi.org/10.1007/s11214-008-9336-1

Auster, U., Glassmeier, K. H., Magnes, W., Aydogar, O., Baumjohann, W., Constantinescu, D., et al. (2008). The THEMIS fluxgate magnetometer. *Space Science Reviews*, *141*(1–4), 235–264. https://doi.org/10.1007/s11214-008-9365-9

Birn, J., Thomsen, M. F., Borovsky, J. E., Reeves, G. D., McComas, D. J., Belian, R. D., & Hesse, M. (1997a). Substorm ion injections: Geosynchronous observations and test particle orbits in three-dimensional dynamic MHD fields. *Journal of Geophysical Research*, *102*(A2), 2325–2341. https://doi.org/10.1029/96JA03032

Birn, J., Thomsen, M. F., Borovsky, J. E., Reeves, G. D., McComas, D. J., & Belian, R. D. (1997b). Characteristic plasma properties during dispersionless substorm injections at geosynchronous orbit. *Journal of Geophysical Research*, *102*(A2), 2309–2324. https://doi.org/10.1029/96JA02870

Birn, J., Thomsen, M. F., Borovsky, J. E., Reeves, G. D., McComas, D. J., Belian, R. D., & Hesse, M. (1998). Substorm electron injections: Geosynchronous observations and test particle simulations. *Journal of Geophysical Research*, *103*(A5), 9235–9248. https://doi.org/10.1029/97JA02635

Blake, J. B., Carranza, P. A., Claudepierre, S. G., Clemmons, J. H., Crain, W. R. Jr., Dotan, Y., et al. (2013). The magnetic electron ion spectrometer (MagEIS) instruments aboard the radiation belt storm probes (RBSP) spacecraft. *Space Science Reviews*, *179*(1-4), 383–421. https://doi.org/10.1007/s11214-013-9991-8

Dai, L., Wang, C., Duan, S., He, Z., Wygant, J. R., Cattell, C. A., et al. (2015). Near-Earth injection of MeV electrons associated with intense dipolarization electric fields: Van Allen Probes observations. *Geophysical Research Letters*, *42*, 6170–6179. https://doi.org/10.1002/2015GL064955

Delcourt, D. C. (2002). Particle acceleration by inductive electric fields in the inner magnetosphere. *Journal of Atmospheric and Solar - Terrestrial Physics*, *64*(5-6), 551–559. https://doi.org/10.1016/S1364-6826(02)00012-3

Dubyagin, S., Sergeev, V., Apatenkov, S., Angelopoulos, V., Runov, A., Nakamura, R., et al. (2011). Can flow bursts penetrate into the inner magnetosphere? *Geophysical Research Letters*, *38*, L08102. https://doi.org/10.1029/2011GL047016

Fu, H. S., Khotyaintsev, Y. V., André, M., & Vaivads, A. (2011). Fermi and betatron acceleration of suprathermal electrons behind dipolarization fronts. *Geophysical Research Letters*, *38*, L16104. https://doi.org/10.1029/2011GL048528

Fu, S. Y., Zong, Q. G., Fritz, T. A., Pu, Z. Y., & Wilken, B. (2002). Composition signatures in ion injections and its dependence on geomagnetic conditions. *Journal of Geophysical Research*, *107*(A10), 1299. https://doi.org/10.1029/2001JA002006

Gabrielse, C., Angelopoulos, V., Runov, A., & Turner, D. L. (2012). The effects of transient, localized electric fields on equatorial electron acceleration and transport toward the inner magnetosphere. *Journal of Geophysical Research*, *117*, A10213. https://doi.org/10.1029/2012JA017873

Gabrielse, C., Angelopoulos, V., Runov, A., & Turner, D. L. (2014). Statistical characteristics of particle injections throughout the equatorial magnetotail. *Journal of Geophysical Research: Space Physics*, *119*, 2512–2535. https://doi.org/10.1002/2013JA019638

Gjerloev, J. W. (2012). The SuperMAG data processing technique. *Journal of Geophysical Research*, *117*, A09213. https://doi.org/10.1029/2012JA017683

Gkioulidou, M., Ohtani, S., Mitchell, D. G., Ukhorskiy, A. Y., Reeves, G. D., Turner, D. L., et al. (2015). Spatial structure and temporal evolution of energetic particle injections in the inner magnetosphere during the 14 July 2013 substorm event. *Journal of Geophysical Research: Space Physics*, *120*, 1924–1938. https://doi.org/10.1002/2014JA020872

Keika, K., Kistler, L. M., & Brandt, P. C. (2013). Energization of O^+ ions in the Earth's inner magnetosphere and the effects on ring current buildup: A review of previous observations and possible mechanisms. *Journal of Geophysical Research: Space Physics*, *118*, 4441–4464. https://doi.org/10.1002/jgra.50371

Kletzing, C. A., Kurth, W. S., Acuna, M., MacDowall, R. J., Torbert, R. B., Averkamp, T., et al. (2013). The Electric and Magnetic Field Instrument Suite and Integrated Science (EMFISIS) on RBSP. *Space Science Reviews*, *179*(1–4), 127–181. https://doi.org/10.1007/s11214-013-9993-6

Kokubun, S., & McPherron, R. L. (1981). Substorm signatures at synchronous altitude. *Journal of Geophysical Research*, *86*(A13), 11,265–11,277. https://doi.org/10.1029/JA086iA13p11265

Liu, J., Angelopoulos, V., Chu, X., Zhou, X., & Yue, C. (2015). Substorm current wedge composition by wedgelets. *Geophysical Research Letters*, *42*, 1669–1676. https://doi.org/10.1002/2015GL063289

Liu, J., Angelopoulos, V., Zhang, X.-J., Turner, D. L., Gabrielse, C., Runov, A., et al. (2016). Dipolarizing flux bundles in the cis-geosynchronous magnetosphere: Relationship between electric fields and energetic particle injections. *Journal of Geophysical Research: Space Physics*, *121*, 1362–1376. https://doi.org/10.1002/2015JA021691

Lui, A. T. Y. (2015). Dipolarization fronts and magnetic flux transport. *Geoscience Letters*, *2*(1), 15. https://doi.org/10.1186/s40562-015-0032-1

Malaspina, D. M., Wygant, J. R., Ergun, R. E., Reeves, G. D., Skoug, R. M., & Larsen, B. A. (2015). Electric field structures and waves at plasma boundaries in the inner magnetosphere. *Journal of Geophysical Research: Space Physics*, *120*, 4246–4263. https://doi.org/10.1002/2015JA021137

Mauk, B. H., Fox, N. J., Kanekal, S. G., Kessel, R. L., Sibeck, D. G., & Ukhorskiy, A. (2013). Science objectives and rationale for the Radiation Belt Storm Probes mission. *Space Science Reviews*, *179*(1–4), 3–27. https://doi.org/10.1007/s11214-012-9908-y

Maynard, N. C., Burke, W. J., Basinska, E. M., Erickson, G. M., Hughes, W. J., Singer, H. J., et al. (1996). Dynamics of the inner magnetosphere near times of substorm onsets. *Journal of Geophysical Research*, *101*(A4), 7705–7736. https://doi.org/10.1029/95JA03856

McPherron, R. L., Russell, C. T., & Aubry, M. P. (1973). Satellite studies of magnetospheric substorms on August 15, 1968: 9. Phenomenological model for substorms. *Journal of Geophysical Research*, *78*(16), 3131–3149. https://doi.org/10.1029/JA078i016p03131

Merkin, V. G., Panov, E. V., Sorathia, K., & Ukhorskiy, A. Y. (2019). Contribution of bursty bulk flows to the global dipolarization of the magnetotail during an isolated substorm. *Journal of Geophysical Research: Space Physics*, *124*, 8647–8668. https://doi.org/10.1029/2019JA026872

Mitchell, D., Lanzerotti, L. J., Kim, C. K., Stokes, M., Ho, G., Cooper, S., et al. (2013). Radiation Belt Storm Probes Ion Composition Experiment (RBSPICE). *Space Science Reviews*, *179*(1–4), 263–308. https://doi.org/10.1007/s11214-013-9965-x

Moore, T. E., Arnoldy, R. L., Feynman, J., & Hardy, D. A. (1981). Propagating substorm injection fronts. *Journal of Geophysical Research*, *86*(A8), 6713–6726. https://doi.org/10.1029/JA086iA08p06713

Motoba, T., Ohtani, S., Gkioulidou, M., Mitchell, D. G., Ukhorskiy, A. Y., Takahashi, K., et al. (2020). Pitch angle dependence of electron and ion flux changes during local magnetic dipolarization inside geosynchronous orbit. *Journal of Geophysical Research: Space Physics*, *125*, e2019JA027543. https://doi.org/10.1029/2019JA027543

Motoba, T., Ohtani, S., Gkioulidou, M., Ukhorskiy, A. Y., Mitchell, D. G., Takahashi, K., et al. (2018). Response of different ion species to local magnetic dipolarization inside geosynchronous orbit. *Journal of Geophysical Research: Space Physics*, *123*, 5420–5434. https://doi.org/10.1029/2018JA025557

Nagai, T. (1982). Observed magnetic substorm signatures at synchronous altitude. *Journal of Geophysical Research*, *87*(A6), 4405–4417. https://doi.org/10.1029/JA087iA06p04405

Nakamura, R., Baumjohann, W., Klecker, B., Bogdanova, Y., Balogh, A., Rème, H., et al. (2002). Motion of the dipolarization front during a flow burst event observed by Cluster. *Geophysical Research Letters*, *29*(20), 3–1–3–4. https://doi.org/10.1029/2002GL015763

Nakamura, R., Baumjohann, W., Mouikis, C., Kistler, L. M., Runov, A., Volwerk, M., et al. (2004). Spatial scale of high-speed flows in the plasma sheet observed by Cluster. *Geophysical Research Letters*, *31*, L09804. https://doi.org/10.1029/2004GL019558

Newell, P. T., & Gjerloev, J. W. (2011). Evaluation of SuperMAG auroral electrojet indices as indicators of substorms and auroral power. *Journal of Geophysical Research*, *116*, A12211. https://doi.org/10.1029/2011JA016779

Nosé, M., Keika, K., Kletzing, C. A., Spence, H. E., Smith, C. W., MacDowall, R. J., et al. (2016). Van Allen Probes observations of magnetic field dipolarization and its associated O+ flux variations in the inner magnetosphere at L < 6.6. *Journal of Geophysical Research: Space Physics*, *121*, 7572–7589. https://doi.org/10.1002/2016JA022549

Ohtani, S., & Gjerloev, J. W. (2020). Is the substorm current wedge an ensemble of wedgelets?: Revisit to midlatitude positive bays. *Journal of Geophysical Research: Space Physics*, *125*. https://doi.org/10.1029/2020JA027902

Ohtani, S., Kokubun, S., Nakamura, R., Elphic, R. C., Russell, C. T., & Baker, D. N. (1990). Field-aligned current signatures in the near-tail region: 2. Coupling between the region 1 and the region 2 systems. *Journal of Geophysical Research*, *95*, 18913. https://doi.org/10.1029/ja095ia11p18913

Ohtani, S., Korth, H., Keika, K., Zheng, Y., Brandt, P. C., & Mende, S. B. (2010). Inductive electric fields in the inner magnetosphere during geomagnetically active periods. *Journal of Geophysical Research*, *115*. https://doi.org/10.1029/2010JA015745

Ohtani, S., Motoba, T., Gkioulidou, M., Takahashi, K., & Singer, H. J. (2018). Spatial development of the dipolarization region in the inner magnetosphere. *Journal of Geophysical Research: Space Physics*, *123*, 5452–5463. https://doi.org/10.1029/2018JA025443

Ohtani, S., Singer, H. J., & Mukai, T. (2006). Effects of the fast plasma sheet flow on the geosynchronous magnetic configuration: Geotail and GOES coordinated study. *Journal of Geophysical Research*, *111*(A1), A01204. https://doi.org/10.1029/2005JA011383

Reeves, G. D., Belian, R. D., Cayton, T. C., Henderson, M. G., Christensen, R. A., McLachlan, P. S., & Ingraham, J. C. (1996). Los Alamos geosynchronous space weather data for radiation belt modeling. In J. Lemaire, D. Heynderickx, & D. Baker (Eds.), *Radiation Belts: Models and standards*, *Geophysical Monograph Series* (Vol. 97). Washington, DC: American Geophysical Union. https://doi.org/10.1029/GM097p0237

Reeves, G. D., Belian, R. D., & Fritz, T. A. (1991). Numerical tracing of energetic particle drifts in a model magnetosphere. *Journal of Geophysical Research*, *96*(A8), 13,997–14,008. https://doi.org/10.1029/91JA01161

Reeves, G. D., Friedel, R. W. H., Henderson, M. G., Korth, A., McLachlan, P. S., & Belian, R. D. (1996). *Radial propagation of substorm injections* (pp. 579–584). Paper presented at Proceedings of the 3rd International Conference on Substorms, ESA SP-389, European Space Agency, France. Retrieved from http://adsabs.harvard.edu/full/1996ESASP.389..579R

Reeves, G. D., Fritz, T. A., Cayton, T. E., & Belian, R. D. (1990). Multi-satellite measurements of the substorm injection region. *Geophysical Research Letters*, *17*(11), 2015–2018. https://doi.org/10.1029/GL017i011p02015

Runov, A., Angelopoulos, V., Gabrielse, C., Zhou, X.-Z., Turner, D., & Plaschke, F. (2013). Electron fluxes and pitch-angle distributions at dipolarization fronts: THEMIS multipoint observations. *Journal of Geophysical Research: Space Physics*, *118*, 744–755. https://doi.org/10.1002/jgra.50121

Runov, A., Angelopoulos, V., Sitnov, M. I., Sergeev, V. A., Bonnell, J., McFadden, J. P., et al. (2009). THEMIS observations of an earthward-propagating dipolarization front. *Geophysical Research Letters*, *36*, L14106. https://doi.org/10.1029/2009GL038980

Runov, A., Angelopoulos, V., Zhou, X.-Z., Zhang, X.-J., Li, S., Plaschke, F., & Bonnell, J. (2011). A THEMIS multicase study of dipolarization fronts in the magnetotail plasma sheet. *Journal of Geophysical Research*, *116*, A05216. https://doi.org/10.1029/2010JA016316

Sergeev, V., Angelopoulos, V., Apatenkov, S., Bonnell, J., Ergun, R., Nakamura, R., et al. (2009). Kinetic structure of the sharp injection/dipolarization front in the flow-braking region. *Geophysical Research Letters*, *36*, L21105. https://doi.org/10.1029/2009GL040658

Sergeev, V. A., Nikolaev, A. V., Tsyganenko, N. A., Angelopoulos, V., Runov, A. V., Singer, H. J., & Yang, J. (2014). Testing a two-loop pattern of the substorm current wedge (SCW2L). *Journal of Geophysical Research: Space Physics*, *119*, 947–963. https://doi.org/10.1002/2013JA019629

Sergeev, V. A., Shukhtina, M. A., Rasinkangas, R., Korth, A., Reeves, G. D., Singer, H. J., et al. (1998). Event study of deep energetic particle injections during substorm. *Journal of Geophysical Research*, *103*(A5), 9217–9234. https://doi.org/10.1029/97JA03686

Sorathia, K. A., Ukhorskiy, A. Y., Merkin, V. G., Fennell, J. F., & Claudepierre, S. G. (2018). Modeling the depletion and recovery of the outer radiation belt during a geomagnetic storm: Combined MHD and test particle simulations. *Journal of Geophysical Research: Space Physics*, *123*, 5590–5609. https://doi.org/10.1029/2018JA025506

Spence, H. E., Reeves, G. D., Baker, D. N., Blake, J. B., Bolton, M., Bourdarie, S., et al. (2013). Science goals and overview of the Energetic Particle, Composition, and Thermal Plasma (ECT) suite on NASA's Radiation Belt Storm Probes (RBSP) mission. *Space Science Reviews*, *179*(1–4), 311–336. https://doi.org/10.1007/s11214-013-0007-5

Takada, T., Nakamura, R., Baumjohann, W., Asano, Y., Volwerk, M., Zhang, T. L., et al. (2006). Do BBFs contribute to inner magnetosphere dipolarizations: Concurrent Cluster and Double Star observations. *Geophysical Research Letters*, *33*, L21109. https://doi.org/10.1029/2006GL027440

Tsyganenko, N. A. (1989). A magnetospheric magnetic field model with the warped tail current sheet. *Planetary and Space Science*, *37*(1), 5–20. https://doi.org/10.1016/0032-0633(89)90066-4

Turner, D. L., Claudepierre, S. G., Fennell, J. F., O'Brien, T. P., Blake, J. B., Lemon, C., et al. (2015). Energetic electron injections deep into the inner magnetosphere associated with substorm activity. *Geophysical Research Letters*, *42*, 2079–2087. https://doi.org/10.1002/2015GL063225

Ukhorskiy, A. Y., Sitnov, M. I., Merkin, V. G., Gkioulidou, M., & Mitchell, D. G. (2017). Ion acceleration at dipolarization fronts in the inner magnetosphere. *Journal of Geophysical Research: Space Physics*, *122*, 3040–3054. https://doi.org/10.1002/2016JA023304

Ukhorskiy, A. Y., Sorathia, K. A., Merkin, V. G., Sitnov, M. I., Mitchell, D. G., & Gkioulidou, M. (2018). Ion trapping and acceleration at dipolarization fronts: High-resolution MHD and test-particle simulations. *Journal of Geophysical Research: Space Physics*, *123*, 5580–5589. https://doi.org/10.1029/2018JA025370

Wygant, J. R., Bonnell, J. W., Goetz, K., Ergun, R. E., Mozer, F. S., Bale, S. D., et al. (2013). The electric field and waves instruments on the radiation belt storm probes mission. *Space Science Reviews*, *179*(1–4), 183–220. https://doi.org/10.1007/s11214-013-0013-7